

Methoxy-bridged tandem CO₂ hydrogenation and ethylbenzene alkylation for selective synthesis of *para*-ethyl-toluene

Xin Shang ^{a,b,1}, Qiao Han ^{a,1}, Wanna Zhang ^{a,1}, Yingxu Wei ^a, Guodong Liu ^{a,*}, Guangjin Hou ^{a,*}, Xiong Su ^{a,*}, Yanqiang Huang ^a, Tao Zhang ^{a,b}

^a Dalian Institute of Chemical Physics, Chinese Academy of Sciences, Dalian, Liaoning 116023, China

^b University of Chinese Academy of Sciences, Beijing 100049, China



ARTICLE INFO

Keywords:
CO₂ hydrogenation
Alkylation
Tandem reaction
Composite catalyst
Aromatics

ABSTRACT

The synthesis of value-added aromatic products, such as *para*-ethyl-toluene (PetT), from the greenhouse gas carbon dioxide (CO₂) and renewable hydrogen (H₂) is greatly desired. However, considerable challenges arise due to complex kinetics and difficulties in arranging multiple active components. Herein, we present a strategy for the selective synthesis of PetT via CO₂ hydrogenation in the presence of ethylbenzene via tandem reactions over a composite catalyst comprising Zn-Zr binary oxide and a modified crystal-stacking HZSM-5 zeolite, achieving over 70% PetT selectivity in the ethyl-toluene (ET) isomers (~80% in the C₅₊ hydrocarbons). State-of-the-art (*quasi*) *in situ* characterizations and corresponding theoretical calculations confirmed the designed reaction route involving stepwise activation of CO₂ to methoxy species and enhanced aromatic cycles for the formation of C-C bonds. And precisely controlled transfer and transformation of intermediate methoxy species contribute to the promoted performance in the selective synthesis of PetT.

1. Introduction

The synthesis of high value-added chemicals, by employing carbon dioxide (CO₂) as a nontoxic and widespread carbon source and green hydrogen (H₂) from renewable energy sources, is of great significance in not only sustainable development of industrial production but also effective mitigation of climate change[1]. Aromatics, traditionally produced via oil routes, could be also obtained by CO₂ hydrogenation; however, of which the selectivity and yield still remarkably suffer from the reverse water gas shift (RWGS) side reaction and the complex aromatization networks driven by both inherent thermodynamics and uncontrollable reaction kinetics[2]. Particularly, it remains a great challenge for exclusively obtaining a single specific aromatic hydrocarbon either through modified Fischer-Tropsch (FT) routes[3,4] or through typical oxygenate-intermediate routes by oxide-zeolite (OX-ZEO) systems[5–7]. For instance, *para*-ethyl-toluene (PetT), one of the most valuable di-alkyl-substituted benzenes which can be dehydrogenated to *para*-methyl-styrene, contributes to an important monomer for the synthesis of various special polymers with superior thermal and mechanic properties[8,9]. Massive production of PetT is still

significantly limited by the poor efficiency and the high energy consumption of separation processes. Shape-selective synthesis from toluene and ethylene/ethanol has been also developed to increase its production in recent years, despite depending on the consumption of valuable raw materials ethylene and ethanol. PetT could be obtained from a direct CO₂ hydrogenation process alternatively, albeit, the typical selectivity of PetT in C₅₊ products is always less than 20% [10–12], indicating a big hurdle in the thermodynamic and kinetics lying on the approach toward preferential production of PetT. Recently, the strategies of introducing specific light aromatics (benzene, toluene, etc.) into CO_x hydrogenation processes have been proposed, which can efficiently change the kinetics by well-regulated tandem reactions for selective synthesis of single aromatic hydrocarbon[11,13–16]. However, the production efficiency is still not satisfactory and few studies on the PetT synthesis involving CO₂ hydrogenation have demonstrated considerable performance so far.

Herein, we report a strategy for selective synthesis of PetT via CO₂ hydrogenation in the presence of ethylbenzene (EB) through tandem reactions coupling the processes of CO₂ hydrogenation to methoxy intermediates and subsequent alkylation over a composite catalyst

* Corresponding authors.

E-mail addresses: gdl@dicp.ac.cn (G. Liu), ghou@dicp.ac.cn (G. Hou), suxiong@dicp.ac.cn (X. Su).

¹ These authors contribute equally

consisting of Zn-Zr binary oxide (ZZO) and a chain-like HZSM-5 zeolite (cZ5) with nano-sheet stacking. Over 70% selectivity of PetT in the ethyl-toluene (ET) isomers (~ 80% in the C₅₊ hydrocarbons) and space time yield (STY) of 24,500 µg g_{cat}⁻¹ h⁻¹ can be achieved at 653 K, 3 MPa with CO₂ conversion of 7.4% and CO from RWGS being suppressed to less than 30%. Ethylene and propylene (> 80%) predominate in the range of C₁₋₅ hydrocarbons with inhibited formation of saturated alkanes. A set of (quasi-) *in situ* characterizations combined with isotopelabeled experiments and theoretical calculations clearly unveil the mechanism of tandem reaction involving stepwise activation of CO₂ to formate and methoxy species, and subsequently transferring and transformation of methoxy for further participating in the C-C coupling reactions within an enhanced aromatic cycle. The introduction of EB significantly changes the reaction kinetics, pointing out the critical role of intermediate transferring in both micro- and nano- scales, which is reflected by the intimacy and acidity effect on the tandem processes. Such a strategy of process design and catalyst fabrication not only afford unprecedented performance in this work, but also will bring comprehensive understanding of other catalytic systems involving numerous competing elementary reactions over multiple active components.

2. Experimental

2.1. Catalyst preparation

Zn-Zr binary oxide (ZnZrO_x) was synthesized by a sol-gel method [15]. Typically, Zr(NO₃)₄•5 H₂O, Zn(NO₃)₂•6 H₂O (molar ratio = 8/1) and citric acid were dissolved in 200 mL deionized water, followed by evaporation at 363 K under stirring until a viscous sol formed. Then, the sol was heated to 453 K for 3 h to form a gel, and calcined at 773 K in air for 6 h.

HZSM-5 zeolite was prepared by a modified hydrothermal method with addition of starch[17]. Briefly, tetraethyl orthosilicate (TEOS), tetra-n-propylammonium hydroxide (TPAOH), Al(NO₃)₃•9 H₂O and H₂O were mixed under stirring. Then, the solution was transferred into a Teflon-lined autoclave and held at 373 K for 3 h. After cooling to room temperature, starch and isopropyl alcohol (IPA) were added into the solution under stirring, followed by further stirring for 24 h in an open container to evaporate the ethanol from hydrolyzation of TEOS. The resulting sol with a molar ratio of 1SiO₂: xAl₂O₃: 0.3TPAOH: 45 H₂O: 0.03IPA (x = 0.01, 0.005, 0.0033, 0.0028) with the addition of 2 g starch per gram SiO₂ was transferred into autoclave for further crystallization at 453 K for 5 days. The crystallized precipitate was collected by filtration, washed by deionized water, dried at 393 K, and calcined at 823 K.

Chemical liquid deposition (CLD) of SiO₂ onto the surface of zeolite was carried out following a reported method[5]. Typically, 1 g zeolite was immersed in 10 mL cyclohexane containing 0.5 mL TEOS. The mixture was refluxed at 353 K under stirring for 2 h, followed by evaporation in vacuum at 333 K. The resulted solid was dried and then calcined at 823 K for 6 h. The CLD procedure was repeated for two times. The zeolites after CLD treatments are denoted as “cZ5” unless otherwise specified.

2.2. Catalyst evaluation

The catalytic tests were conducted in a continuous flow fixed-bed stainless steel reactor (inner diameter of 10 mm) with a K-type thermocouple located at the center of the catalyst bed. Generally, ZnZrO_x and zeolite composite catalysts were prepared by physical mixing. The powder of ZnZrO_x and zeolite were grinded in an agate mortar for 10 min. The mass ratio of ZnZrO_x and zeolite was 1: 1 unless otherwise stated. For studying the intimacy effect, ZnZrO_x and zeolite were pressed separately, crushed and sieved to 20–40 or 60–80 meshes. Then, the granules of the two samples as well as quartz sand (20–40 meshes) were mixed homogeneously by shaking in a vessel. About 250 mg catalyst

granules and 1 g quartz sand were mixed and loaded into the reaction tube. The catalysts were reduced in H₂ (30 mL min⁻¹) at 723 K for 2 h under atmospheric pressure before testing. After cooling to reaction temperature, the mixture gas with a composition of CO₂/H₂/Ar (23/69/8, vol%) was introduced into the reactor. For the coupling reaction with ethylbenzene (EB), EB was injected by a constant flow pump. The whole effluents after reactions were analyzed online using two tandem Agilent 7890B gas chromatographs. The inorganic products and methane were analyzed by a thermal conductivity detector (TCD) equipped with TDX-01 column and the hydrocarbons were analyzed by a flame ionization detector (FID) equipped with HP-PONA column. Methane is acted as bridge to associate the results of TCD and FID. The carbon balance is 90%–110% for all the cases in this work.

The conversion of CO₂ and selectivity of CO were calculated according to:

$$Conv_{CO_2} = \frac{CO_{2outlet} - CO_{2inlet}}{CO_{2inlet}}$$

$$Sel_{CO} = \frac{CO_{outlet}}{CO_{2inlet} - CO_{2outlet}}$$

where the subscripts “inlet” and “outlet” represent chemicals in the inlet and outlet, respectively.

Hydrocarbon products distribution was calculated according to:

$$Sel_{C_nH_m} = \frac{nC_nH_{moutlet}}{\sum nC_nH_{moutlet} - 8EB_{outlet}}$$

C_nH_{moutlet} means the mole of individual hydrocarbon at the outlet.

Aromatics (C₅₊) distribution was calculated according to:

$$Sel_{Aro} = \frac{Aro}{\sum Aro_{outlet} - EB_{outlet}}$$

2.3. Catalyst characterizations

Powder X-ray diffraction (XRD) patterns were acquired by a PW3040/60 X'Pert ProSuper (PANalytical) diffract meter equipped with Cu K α radiation source, operating at 40 kV, 40 mA. High resolution transmission electron microscopy (HRTEM) images were taken on a JEM2100 microscope, operating at an accelerating voltage of 200 kV. The surface area and pore distribution of the catalysts were measured by N₂ physical adsorption desorption on an ASAP 2460 Quantachrome instrument. The samples were degassed at 573 K in vacuum for 6 h prior to the measurement. Temperature-programmed desorption of NH₃ (NH₃-TPD) was conducted on a Micromeritics AutoChem II 2920 chemisorber. Before the measurement, the samples were purged in He stream at 773 K for 30 min and then cooled down to 373 K for NH₃ adsorption. Then, the gas was switched to He, followed by heating to 1073 K with a ramping rate of 10 K min⁻¹.

Infrared spectroscopy with pyridine adsorption (Py-IR) and 2,6-Di-tert-butylpyridine adsorption (2,6-DTBPy-IR) was carried out on a BRUKER Equinox 55 spectrometer in a transmission mode with a resolution of 4 cm⁻¹ at 4000–400 cm⁻¹ range. The samples were pressed into wafers and pretreated under dynamic vacuum at 773 K for 30 min. For pyridine adsorption, the pyridine vapor was introduced to the sample for 1 min after the sample cooling to 323 K. Then, the IR spectrum was collected after evacuation at 423 K, 623 K, 723 K, respectively. For 2,6-Di-tert-butylpyridine, the vapor was introduced to the sample at 423 K for 10 min, and the IR spectrum was collected after vacuum treatment for 0.5 h.

In situ diffuse reflectance infrared Fourier transform (DRIFT) spectra were acquired using a Bruker Vertex 70 spectrometer equipped with a mercury cadmium telluride (MCT) detector, recorded with a resolution of 4 cm⁻¹. Prior to the *in-situ* reaction, the samples were treated in the DRIFT cell under a H₂ flow (30 mL min⁻¹) at 773 K for 1 h, followed by purging with a He flow at the same temperature for 30 min. After

cooling to 623 K, a background spectrum was collected, following which the He flow was switched to a CO₂/H₂/Ar (23/69/8, vol%) flow (10 mL min⁻¹). Then, the EB was introduced into the system by a CO₂/H₂/Ar carrier flow. For TPD-DRIFTS test, the samples were exposed to methanol or methanol + EB mixture gas for 10 min at 298 K, followed by purging under He atmosphere for 30 min. Then, the temperature was raised from 373 K to 673 K at a rate of 14 K min⁻¹. In the meanwhile, the IR patterns were recorded every 13 seconds.

Retained species in spent catalysts were occluded by a reported method[18] with a home-made instrument. Typically, 100 mg catalysts were loaded in a U-shape reactor and pretreated in a 20 mL min⁻¹ H₂ flow at 673 K for 0.5 h, then going through reactions once introducing the gaseous and liquid feedstock under specific conditions. After a certain period of reaction time, the reactor was kept away from heater and immediately quenched by liquid nitrogen. The catalysts were purged for 5 min in He to exclude the weakly adsorbed species. Then, the catalysts were solved in 10% HF solution and extracted by CH₂Cl₂. The extracted organic species were analyzed by GC-MS (Agilent 8890–7250) equipped with an HP-5 chromatographic column (60 m × 250 μm × 0.25 μm). The peak of GC-MS spectra was identified using the NIST database.

The samples for *quasi in situ* NMR experiments were prepared by a similar method as that for retained species. The spent catalysts did not go through sweeping and solving steps, but directly transferring into a sample tube for subsequent NMR experiments. The one-dimensional (1D) ¹H spin-echo, ¹³C single pulse, ¹³C cross-polarization (CP) and 2D ¹H–¹³C heteronuclear correlation (HETCOR) NMR experiments were performed by using a 4 mm double-resonance probe with a magic angle spinning (MAS) speed of 10 kHz on a 9.4 T Bruker Avance NEO 400 spectrometer, with the Larmor frequencies of ¹H and ¹³C at 399.8 and 100.5 MHz, respectively. ¹H and ¹³C chemical shifts are referenced to adamantane at 1.74 ppm and 38.5 ppm, respectively. ¹H spin-echo NMR spectra were recorded with a π/2 pulse of 70 kHz and recycle delay of 3 s for 256 scans accumulating. A π/2 pulse of 60 kHz with recycle delay of 10 s were used to collect the ¹³C single pulse NMR spectrum. For the ¹³C CP experiment, the contact pulses for ¹H and ¹³C were set to 62 and 74 kHz, respectively, with contact time of 3000 μs and recycle delay of 2 s. 2D ¹H–¹³C HETCOR NMR spectrum was recorded using 160 scans for each of the 40 points in t1 dimensions with an increment time of 100 μs. The other acquisition parameters were set the same as the ¹³C CP experiment. Spinal64 1 H decoupling with about 80 kHz was applied during all the ¹³C acquisitions.

2.4. Theoretical calculations

In this work, the cluster model (72 T) of H-ZSM-5 catalyst was taken from the crystallographic MFI structure of the International Zeolite Association. As shown in Fig. S21, the terminal Si–H was fixed with the bond length of 1.47 Å oriented along the direction of the corresponding Si–O bond. The substituted Al atom was placed at the T12 site and Al12–O24H-Si12 site was chosen to represent the Brønsted acid site for H-ZSM-5, accessible to the adsorbed molecules.

A combined theoretical approach, namely ONIOM[19] (ωB97XD/6–31 G(d, p):AM1), was employed in the geometry optimization and frequency calculation. For the 72 T cluster of H-ZSM-5, the local structure of 24 T around the Al center and the adsorbed species were set to the high layer, while the rest of atoms were set to the low layer. During the geometry optimization, the atoms in high layer were relaxed, the atoms in low layer were fixed in the crystallographic data. Various adsorption structures and transition states (TS) were predicted using the ONIOM methods. The ωB97XD method, a long-range corrected hybrid DFT for dispersion developed by Chai and Head-Gordon, can describe long-range dispersion interactions on zeolites catalytic system [20]. During the frequency calculations, only a single imaginary frequency was observed for the transition state, and no imaginary frequency was observed for the adsorbed state. The intrinsic free energies

barriers (ΔG^\ddagger) at 633 K for formation and transformation of SMS were obtained from the ωB97XD total electronic energies and the thermal correction from the ωB97XD/6–31 G(d,p):AM1 frequency calculations. Furthermore, on the basis of optimized structures, the single-point energies were calculated at the level of ωB97XD/6–31 G(d, p). The energies have been corrected for zero-point vibration energies. All calculations were performed using the Gaussian 09 software package [21].

The adsorption enthalpies (ΔH_{ads}) and free energies (ΔG_{ads}) were calculated as: $\Delta H_{\text{ads}} = H_{\text{complex}} - H_{\text{zeolite}} - H_{\text{adsorbate}}$, where H_{complex} , H_{zeolite} , $H_{\text{adsorbate}}$ refer to calculation energies of the system of the adsorbed species (Methanol/EB) inside zeolite, the zeolite and the adsorbed molecule, respectively.

3. Results and discussion

3.1. Characterization of catalysts

The synthesis of ET from CO₂ hydrogenation in the presence of EB is realized by a continuous fix-bed reactor packed with composite catalysts consisting of ZZO and cZ5 zeolite. ZZO is prepared via a sol-gel method according to a previous study[15]. It shows a tetragonal type of ZrO₂ structure according to XRD pattern without detectable signals of Zn species, suggesting good dispersion of Zn in binary oxide[22] (Fig. S1). cZ5 zeolite is synthesized by a modified hydrothermal method with an addition of starch[17], giving a nanocrystal-stacking structure as shown in TEM and SEM patterns (Figs. S2–3) with typical MFI topology and micropores (Figs. S4–5). To eliminate the isomerization side reactions on the surface acid sites, the zeolite moiety is also subjected to SiO₂ modification following a conventional chemical liquid deposition approach[5] (details in Method section), as characterized by 2, 6-Di-tert-butylpyridine adsorption infrared spectra (Fig. S6).

3.2. Catalytic performance

Generally, the synthesis of hydrocarbons from CO₂ hydrogenation is greatly affected by the reaction conditions, such as temperature, pressure and contact time of reactants on the surface of catalysts, in regard to the intertwined thermodynamic and kinetic factors. Fig. 1a exhibits the dependent performance of CO₂ hydrogenation in the presence of EB on the reaction temperature from 593 K to 673 K. As the CO₂ conversion gradually increases from 1.9% to 9.6%, the selectivity of CO, generated from RWGS side reaction, also rises from 17.6% to 32.5%, which could be rationalized by the endothermic nature of RWGS. In addition, C_{1–5} products also slightly increase with increasing temperature possibly due to the partial decomposition of EB and certain aromatic products (Fig. S11). This result is consistent with the selectivity of ET decreasing as the proportion of benzene, toluene and xylene products increases, which may also result from the decomposition of EB and subsequent alkylation (Fig. S11). Such side reactions not only pose an obstacle for the separation of target product, but also consume the effective alkylation intermediates, thus should be suppressed. Fortunately, the CO₂ hydrogenation atmosphere has an inhibiting effect on the decomposition reaction in this work (Fig. S12), while optimized temperature could also contribute to the higher selectivity. An ET selectivity of 86% could be obtained at 593 K with a slight decrease to 82.4% even at 653 K. In the meanwhile, the high-level selectivity of *para*-isomer PetT account for 72.5% in all ET isomers, which is far beyond the value of thermodynamic equilibrium (Fig. S13). On the other hand, lower pressure can give a higher selectivity of PetT (~ 80%) (Fig. 1b), which might be attributed to the facile desorption of products rather than isomerization over acidic sites. However, such low pressure also causes the higher fraction of CO and more severe decomposition of EB, as well as reduced efficiency of the CO₂ conversion. Increasing GHSV from 6000 to 12,000 mL g⁻¹ h⁻¹, also indicating a shorter contact time, as shown in Fig. 1c, demonstrates a positive effect on the ET and PetT

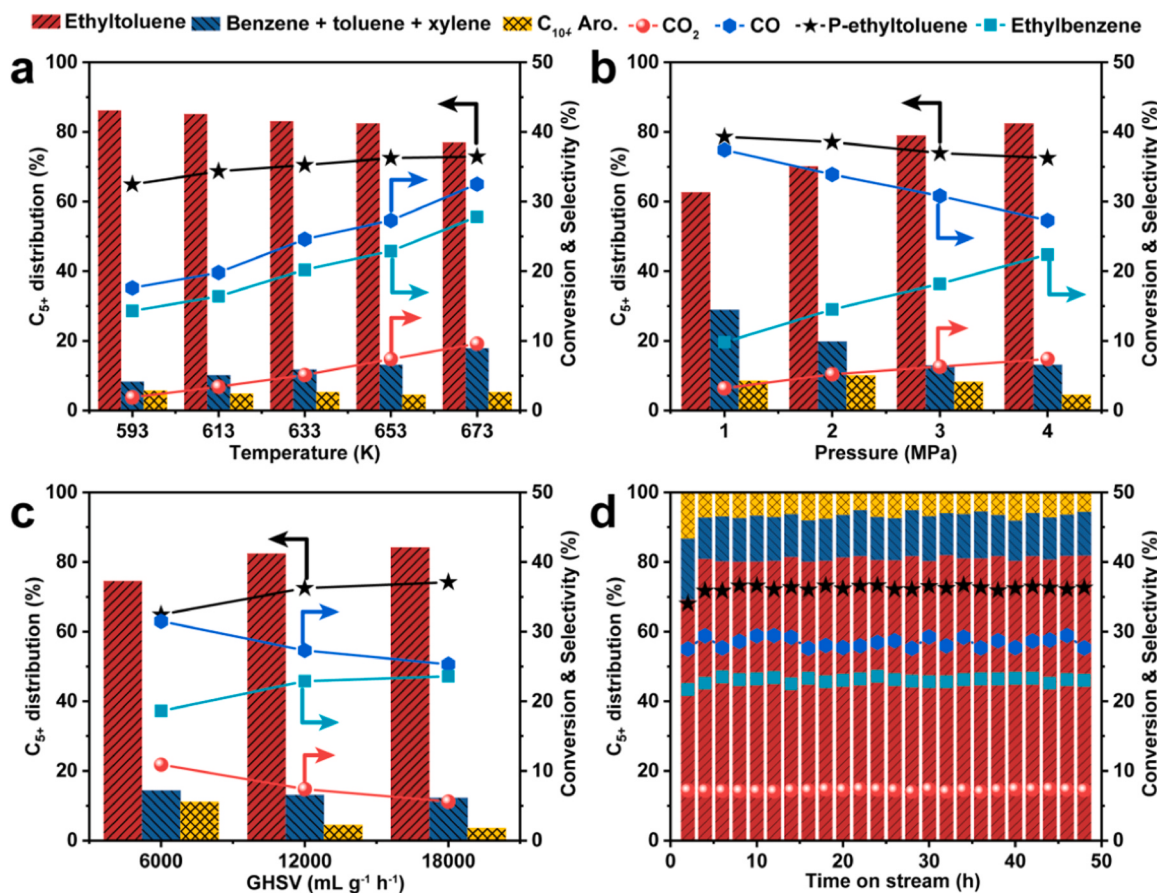


Fig. 1. The dependent conversion and product distribution on (a) Temperature, (b) Pressure, (c) Gaseous hourly space velocity (GHSV). (d) Stability test. Reaction conditions: 633 K, 3 MPa, GHSV of a mixture gas ($\text{CO}_2/\text{H}_2/\text{Ar} = 23:69:8$, vol%) = $12,000 \text{ mL g}^{-1} \text{ h}^{-1}$, and WHSV of EB = 1 h^{-1} .

selectivity (both improved by 10%). This suggests faster transferring of reactants and products might relatively favor the kinetics of target reactions. The conversions of EB and CO_2 have a positive correlation with the temperature and pressure changing. This result is reasonable as increased CO_2 conversion leads to higher yield of methoxy species, which can promote the alkylation of EB. In contrast, the change of GHSV gives a negative correlation between the conversions of EB and CO_2 . That is caused by the increased proportion of CO release, resulting in lower yield of methoxy species. In fact, the introduction of EB significantly changes the products distribution to the case that more carbon atoms are incorporated into aromatic products (Fig. S14). We further carried out a 50-hour stability test and found that both of CO_2 conversion and Pett selectivity maintained at a consistent level during the whole trial, that are $\sim 8\%$ and $\sim 75\%$, respectively (Fig. S15). The carbon deposition is measured to be as low as 3% of total weight according to a thermogravimetry test for spent catalyst (Fig. S16). The reaction conditions featuring short contact time and hydrogen atmosphere, as well as the inherent durability of Zr-based oxide (Fig. S17) component [22,23] and well-designed zeolite component should contribute to such stability, further suggesting a potential industrial application.

3.3. Identification of the reaction pathway

To figure out the reaction pathway, we carried out the CO_2 conversion tests and monitored the surface of catalysts by *in situ* diffuse reflectance infrared Fourier transform (DRIFT) spectra. As for CO_2 hydrogenation over ZZO + cz5 composite catalyst (Fig. 2a), the characteristic peaks of formate (HCOO^*) at 2973 cm^{-1} and 2883 cm^{-1} in C-H vibration region as well as 1584 cm^{-1} and 1356 cm^{-1} in C-O vibration region [22,24] emerged and increased over time in the initial stage and

followed by a plateau, suggesting a possible reaction equilibrium of HCOO^* species. In the meanwhile, the appeared peaks of methoxy (CH_3O^*) at 2936 cm^{-1} , 2836 cm^{-1} and 1462 cm^{-1} attributed to the C-H vibration [24], as well as those at 1062 cm^{-1} and 1038 cm^{-1} attributed to the C-O vibration [25] manifest the deep hydrogenation of HCOO^* . Such surface species have also been observed on ZZO + S-1 (siliceous MFI zeolite) without considerable acid sites (Fig. 2b), indicating that ZZO is responsible for the CO_2 hydrogenation via a HCOO^* to CH_3O^* to CH_3OH pathway, as observed in other related ZnZr-based systems [13,22]. Interestingly, although the peak intensity of HCOO^* (1584 cm^{-1}) for ZZO + cz5 and ZZO + S-1 is quite similar (Fig. 2c), the peak intensity of CH_3O^* (1038 cm^{-1}) for ZZO + cz5 is significantly lower than that for ZZO + S-1. This might be attributed to the consumption of methoxy species over acid sites in cz5. The characteristic peaks of HCOO^* and CH_3O^* are still maintained even after the introduction of EB, while the peaks of aromatic hydrocarbon at $\sim 1500 \text{ cm}^{-1}$ gradually increase (Figs. 2d and 2e). However, the intensity of HCOO^* (1584 cm^{-1}) exhibits a substantial reduction for ZZO + cz5 after the introduction of EB (Fig. 2f), while only a slight variation of the HCOO^* peak is observed on ZZO + S-1. We speculate that EB rapidly consumed the alkylation species over acid sites in cz5, which kinetically propelled the transformation of HCOO^* intermediates. Such kinetic promotion would not occur in the absence of acid sites as for S-1. These results indicate a close interplay between hydrogenation and alkylation in this tandem process.

In situ $^{13}\text{CO}_2$ hydrogenation experiments combined with solid state nuclear magnetic resonance (ssNMR) and gas chromatography-mass spectrometry (GC-MS) technologies have been further conducted, confirming that CO_2 engaged in the production of PetT. Two-dimensional (2D) $^1\text{H}-^{13}\text{C}$ heteronuclear correlation (HETCOR) magic angle spinning (MAS) NMR spectra (Fig. 3a) clearly demonstrate the species of

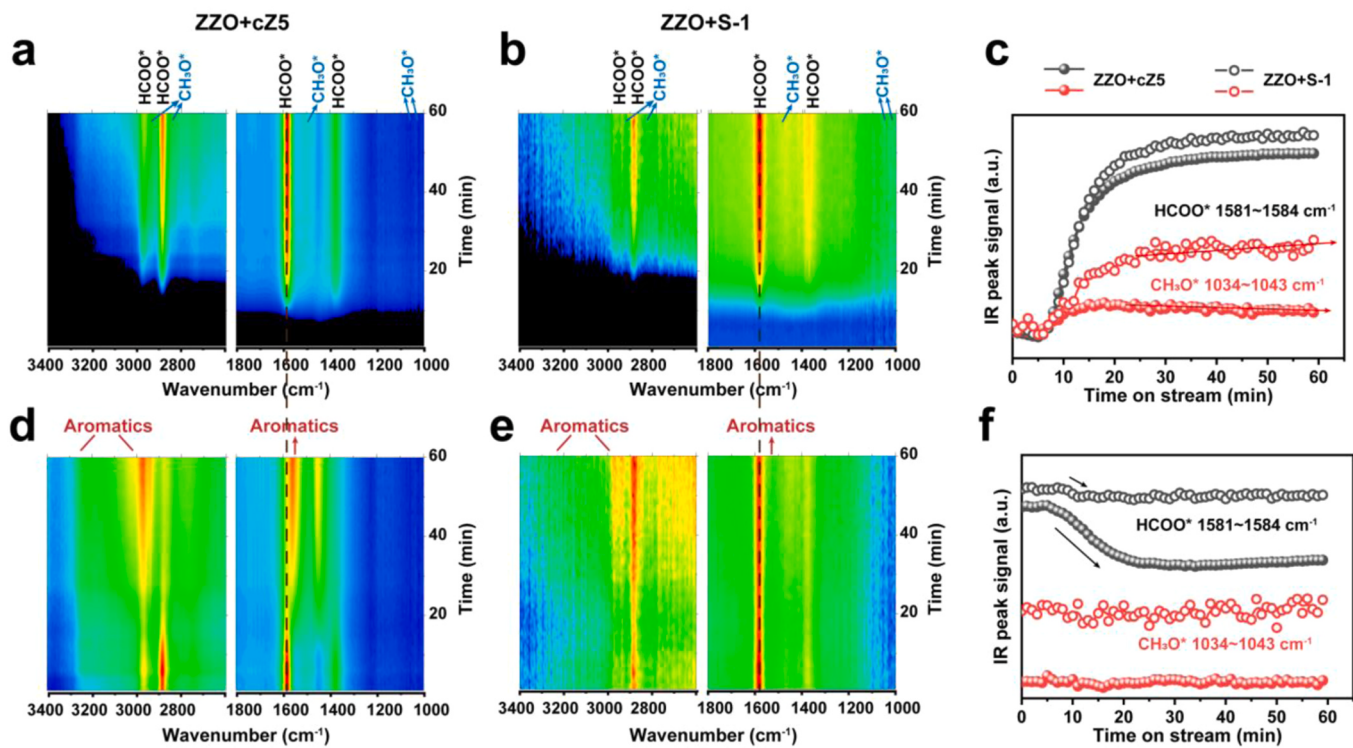


Fig. 2. *In situ* DRIFTS of CO₂ hydrogenation over (a) ZZO + cZ5 and (b) ZZO + S-1, CO₂ hydrogenation followed by the introduction of EB over (d) ZZO + cZ5 and (e) ZZO + S-1. The change of surface species over time based on IR peaks in (c) CO₂ hydrogenation and (f) CO₂ hydrogenation followed by the introduction of EB. Reaction conditions: 623 K, 0.1 MPa, mixture gas (CO₂/H₂/Ar = 23:69:8, vol%) = 20 mL min⁻¹, EB was carried by mixture gas through a bubbler.

HCOO* and CH₃O* with ¹³C signals at ~170 and ~50 ppm, respectively [26], in ¹³CO₂ hydrogenation. Further co-feeding the EB (Fig. 3b), a significant amount of saturated alkyl aromatics species are produced, which can be evidenced by the correlation signals with ¹³C at ~19 ppm and ¹H at ~2.2 / 7.4 ppm, corresponding to the correlation between the alkyl group and hydrogen in aromatic rings (¹H ~ 7.4 ppm)[27]. The retained species in the spent catalysts also exhibit the apparent transformation of EB toward ET with higher fraction of *meta*-ethyl-toluene (MetT) due to the larger molecule size (Fig. 3c), whereas the spent catalysts after ¹³CO₂ hydrogenation without EB show negligible aromatic products and even no other hydrocarbons generated from C-C coupling reactions. These results not only indicate a remarkably improved efficiency of C-C coupling in the case that EB is introduced, but also suggest that CO₂ hydrogenation contributes to the target products by supplying the alkylation intermediates rather than directly forming hydrocarbons. It is worth noting that the significant shift of MS peaks of PetT compared with that in natural abundance. The peak at 120 is almost completely shifted to 121, suggesting that more than 95 molar percent of PetT molecules have a single ¹³C atom. The peak of a moiety of PetT at 105, which is attributed to a toluene ion, is shifted to 106, further pointing that the labeled atom should be attached to the aromatic ring as a methyl. All above results clearly demonstrate a reaction pathway that CO₂ is hydrogenated to CH₃O* species via HCOO* intermediate, followed by kinetic favored alkylation reaction with introduced EB instead of self C-C coupling between each other, leading to the formation of methyl attached to the aromatic ring and finally the preferential synthesis of ET and PetT target products.

3.4. Evolution of the key intermediates

Although we have depicted the reaction pathway and found out the key intermediates by the means of various *in situ* characterizations, tracing the dynamic evolution of intermediates is still challenging, despite its great significance in such a multi-component system for

effective tandem reactions. Thanks to the excellent capability of ssNMR to detect hydrogen and carbon elements, we can discriminate various methoxy-related species over different active sites[26–28] (Fig. 4a-f and Fig. S18). The signals in the range of 45 ~ 65 ppm can be reasonably deconvoluted into five types of methoxy species, corresponding to the free methanol species at about 49 ppm[26,27,29], methoxy species over Zn-Zr oxide at 52 ~ 54 ppm[26], dimethyl ether species at above 60 ppm[29], and surface methoxy species (SMS) over bridged Si-O-Al at around 58 ppm formed by interacting with Brønsted acid sites[27–29], respectively. As for CO₂ hydrogenation without EB (Fig. 4g), the fraction of free methanol gradually increases with extended reaction time from 1 min to 15 min accompanied by the consumption of methoxy over Zn-Zr oxide, suggesting the hydrogenation of methoxy to methanol over Zn-Zr oxide. In the meanwhile, dimethyl ether and SMS species significantly accumulate over time, which is closely related to the acid-catalyzed dehydration in the zeolite. In contrast, the accumulation of dimethyl ether is relatively lower for CO₂ hydrogenation in the presence of EB, as the higher fraction of free methanol species is retained. Such differences imply that the introduction of EB contributes to the favored consumption of SMS species, and therefore the equilibrium is shifted from dimethyl ether to SMS, resulting in reduced proportion of dimethyl ether species (Fig. 4h). Given that SMS is considered to be one of the key active intermediates for methanol to hydrocarbon reactions at the initial stage[29], we speculate that C-C coupling between EB and SMS possesses much higher intrinsic reaction rate, so that the primary C-C coupling with extremely high kinetic barrier and the complex reaction networks, such as olefin- and oxygenate-based cycles reported in conventional CO_x hydrogenation or methanol transformation processes[27,30], are therefore circumvented. As a result, the side reactions toward CO and non-aromatic hydrocarbons are well suppressed with much higher carbon efficiency of CO₂ hydrogenation.

We also carried out the temperature-programmed desorption (TPD) of methanol + EB (Fig. 4i) and methanol (Fig. 4j) in conjunction with DRIFTS over the composite catalyst (Fig. S19), since methanol is deemed

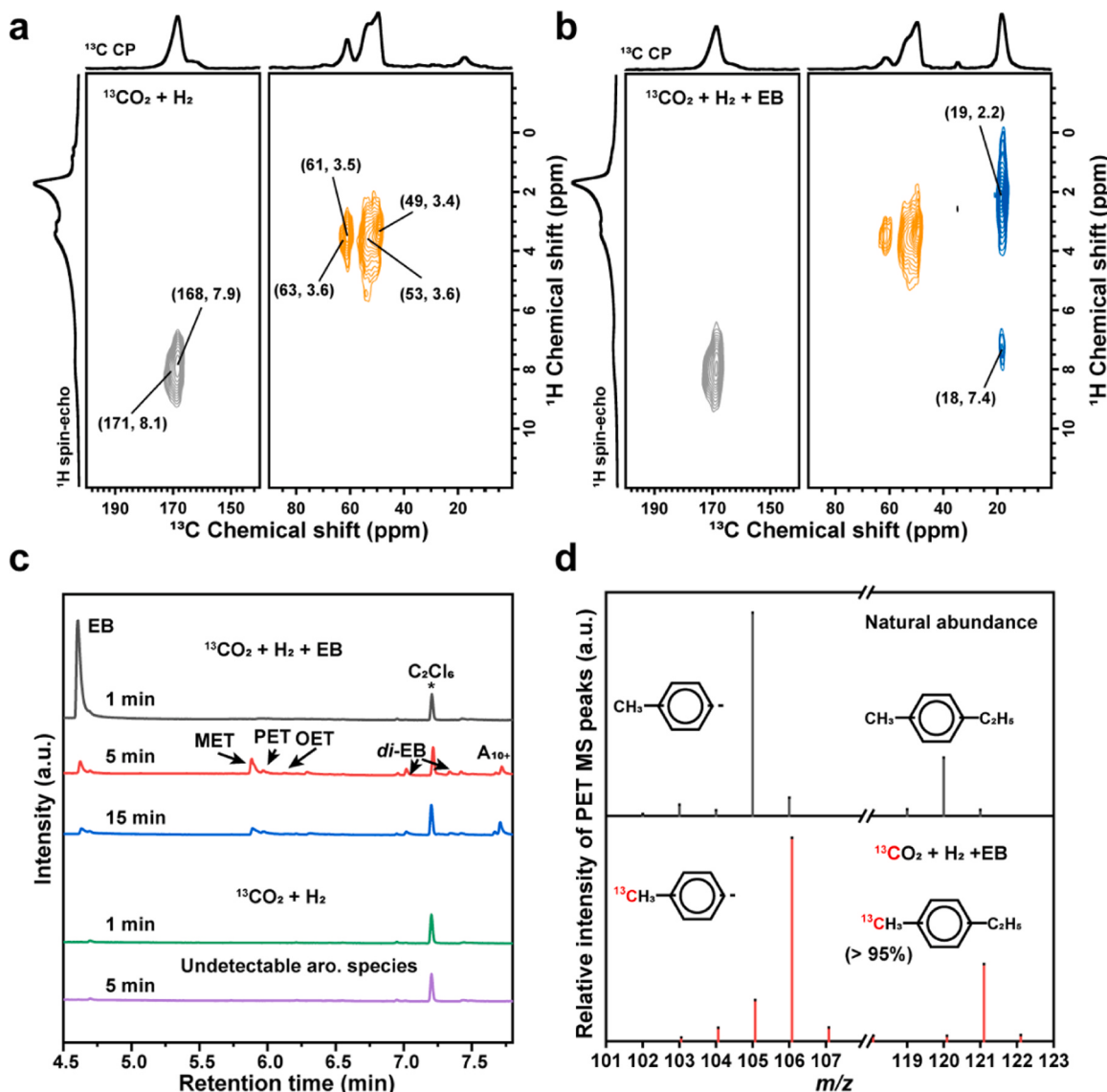


Fig. 3. Two-dimensional (2D) ¹H-¹³C heteronuclear correlation (HETCOR) magic angle spinning nuclear magnetic resonance (MAS NMR) spectroscopy results for (a) ¹³CO₂ + H₂, (b) ¹³CO₂ + H₂ in the presence of EB in natural abundance. (c) Gas chromatography-mass spectrometry (GC-MS) results of species occluded in spent catalysts after ¹³CO₂ hydrogenation with/without EB for different time. (d) MS peaks of target product PetT after ¹³CO₂ hydrogenation with EB in comparison with that of natural abundance. Reaction conditions: 573 K, 3 MPa, CO₂/H₂ = 1/3, EB was introduced by a bubbler.

to be the bridge intermediate in the tandem reactions. Different from the CO₂ hydrogenation system, these TPD processes feature much higher concentration of methoxy in the initial time. However, apparent peaks of surface methoxy species over Brønsted acid sites[29] at 940, 2889 and 2977 cm⁻¹ do not emerge until the temperature is raised up to 523 K for methanol-only case and 549 K for methanol + EB case, while the peaks of methanol (1006, 1031 and 1057 cm⁻¹) decrease significantly once increasing the temperature from 393 K. This suggests the formed SMS at initial stage might be consumed to generated hydrocarbons, which are also shown in the DRIFTS results, or coupling with neighboring EB molecules (Fig. 4k). The later emergence of SMS in the EB containing system indicates a higher fraction of SMS engaging in the transformation, further giving the evidence of kinetically favored coupling reactions between EB and SMS.

3.5. Effect of the intermediate transfer

Inspired by the insight into the dynamic evolution of methoxy species, we notice the distinct reaction kinetics of CO₂ hydrogenation in the

presence of EB, which exhibits a much more favored C-C coupling. Intuitively, as the SMS over acid sites in zeolite could be consumed rapidly, the migration of methoxy species from oxide to zeolite would be another hindrance for the whole tandem process. Therefore, we performed CO₂ hydrogenation in the presence of EB over composite catalysts with different intimacy of components, which comprised oxide and zeolite in the granularity of 20–40 mesh, 60–80 mesh and sub-micrometer powder (Fig. 5a). Differences in granularity render varied communication distances with two orders of magnitude gap for mass transfer[31]. As a result, the CO₂ reaction rate exhibits a significant escalating trend with shortened distance, which could be rationalized by the enhanced intermediate transfer from oxide surface to acid sites inside zeolite channels. Interestingly, under the same reaction conditions, CO₂ reaction rate demonstrates a smaller increase without the introduction of EB, although the closer intimacy literally favors the CO₂ hydrogenation as well. We speculate that in the presence of EB, the effect of intermediate transfer on the CO₂ hydrogenation is more significant, as the timely supply of methoxy species adequately satisfies the demand of EB alkylation, thereby steering the whole reaction positively

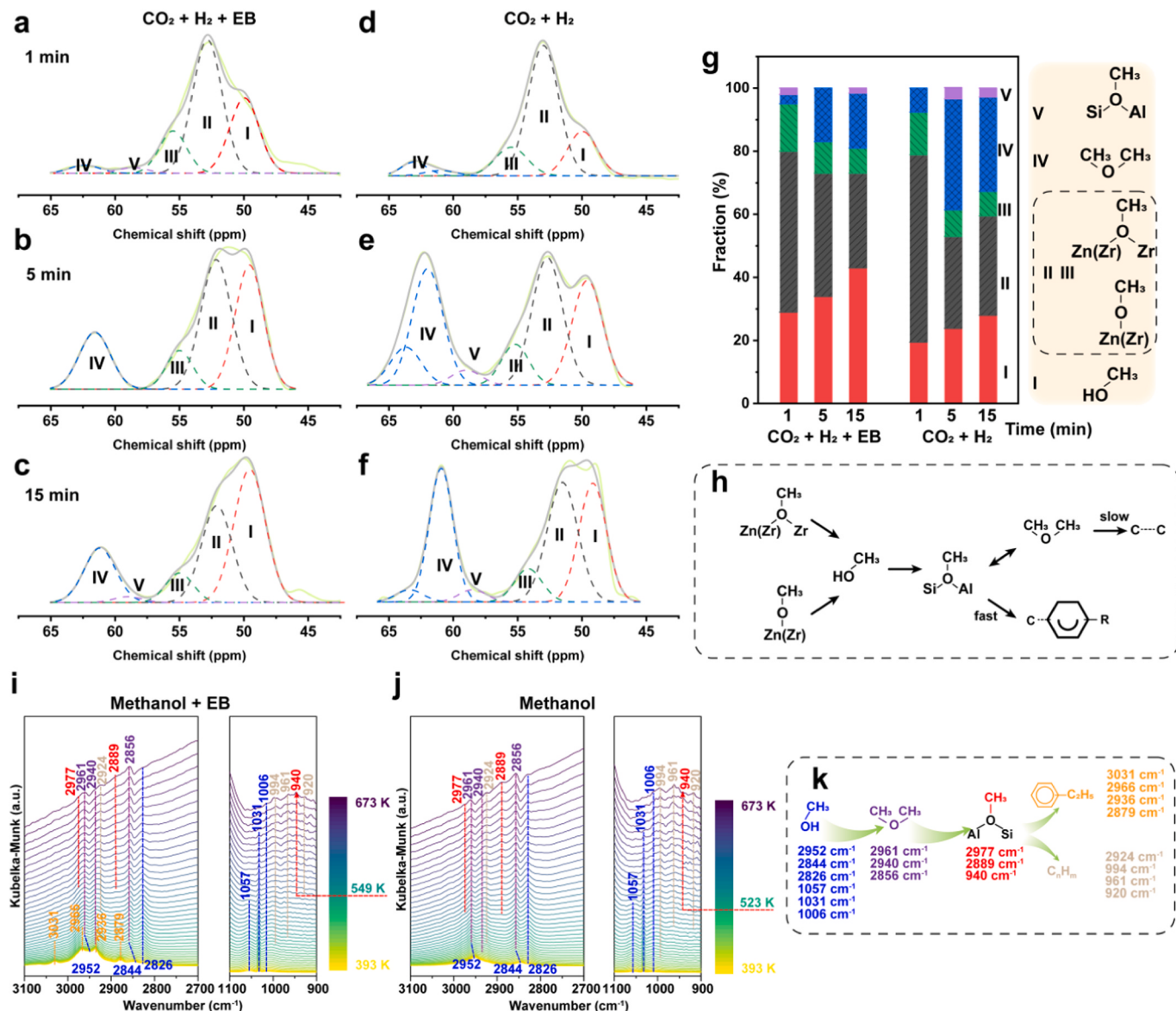


Fig. 4. Deconvoluted high-power decoupling ¹³C NMR signals of methoxy-related species during ¹³CO₂ hydrogenation with EB for (a) 1 min, (b) 5 min, (c) 15 min, and without EB for (d) 1 min, (e) 5 min, (f) 15 min. (g) The fraction of different methoxy-related species and (h) their proposed evolution pathway obtained based on ¹³C NMR signals. Conditions: 573 K, 3 MPa, CO₂/H₂ = 1/3, EB was introduced by a bubbler. *In situ* temperature programmed desorption (TPD)-DRIFTS of i methanol + EB and (j) methanol. (k) proposed evolution pathway based on TPD-DRIFTS.

toward the target products. In contrast, in the absence of EB, CO₂ hydrogenation faces a bottleneck not only in the mass transfer between two components, but also in the C–C coupling inside zeolite. Moreover, such promotion of catalytic performance by facilely regulated intimacy would not lead to excessive hydrogenation due to the closer contact between different active sites and iterative reactions of key intermediates, as reported in some CO_x hydrogenation systems [6,32], and therefore afford higher adjustability of this process.

Besides at the micrometer scale, we also performed the trials with composite catalysts comprising zeolite with varied Si/Al ratio (SAR) to investigate the effect of intermediate transfer from a view of nanoscale (Fig. 5b). The increased SAR, indicating lower acid density (Fig. S20), gives reduced CO₂ conversion and ET selectivity with higher fraction of benzene, toluene and xylene from ~ 13% to ~ 24%. As mentioned above, these undesired products are formed through the decomposition of EB, a unimolecular reaction that potentially occurs over the acid sites and is even promoted by the H₂ atmosphere (Fig. S9). Based on our discovery in the evolution of intermediate species, SMS also occupy the

acid sites. In addition to reacting with EB via C–C coupling, they also have potential competition with EB molecules at the adsorption sites. As for zeolite with higher acid density, EB molecules tend to be alkylated by neighboring SMS because of the closer spatial distance and sluggish C–C coupling between SMS each other. In contrast, for zeolite with lower acid density, there would be a much longer distance for intermediate transferring and encountering with each other to participate in a bimolecular reaction to form ET products. On the contrary, a considerable number of EB molecules are subjected to decomposition and subsequent alkylation, resulting in various side products (Fig. 5c). It is worth noting that a number of systems involving CO_x hydrogenation to aromatics suffer from activity-selectivity trade-off due to the excessive hydrogen transfer catalyzed by strong Brønsted acid sites [7,23], which consumes the active olefin intermediates and makes the tandem reaction have to be conducted over a zeolite with high SAR, further reducing the efficiency of CO₂ and intermediate transformation in return. In this work, such an activity-selectivity trade-off might be circumvented by reinforced intermediate transfer and well-designed reaction pathway, in

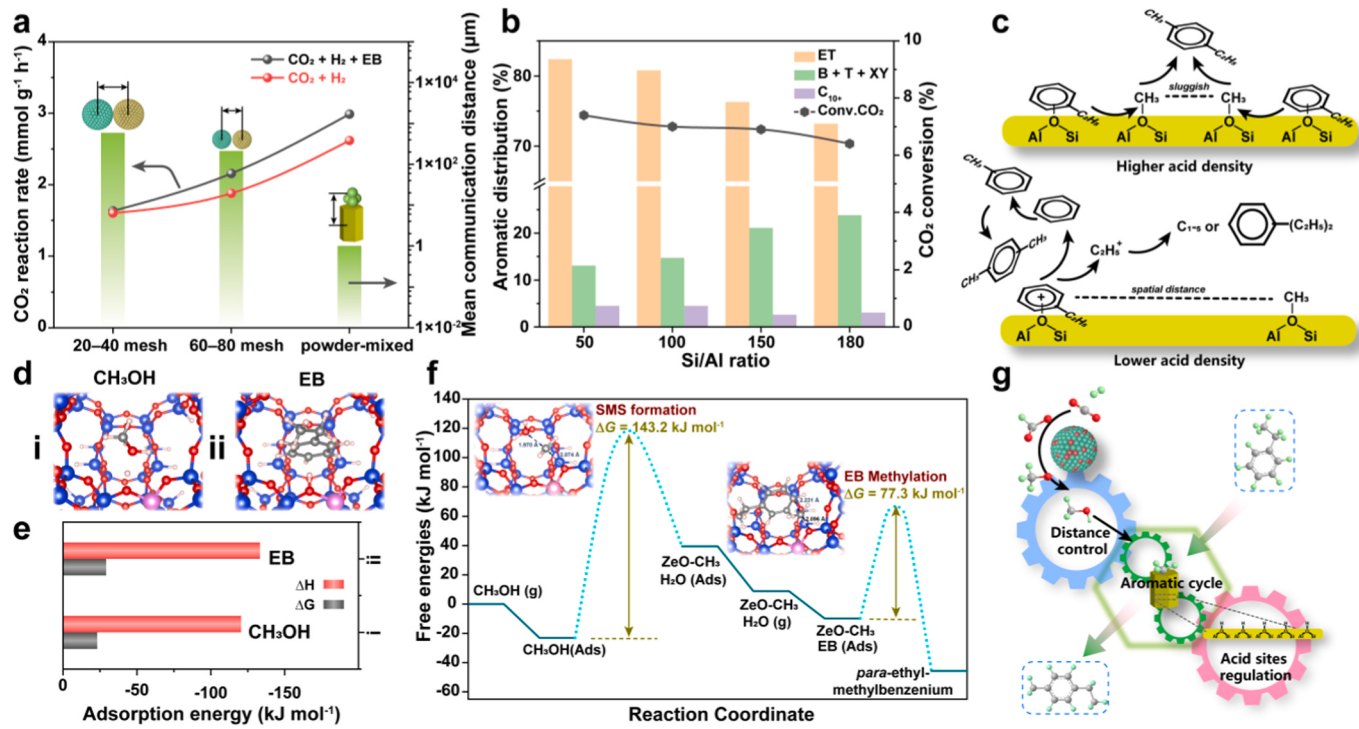


Fig. 5. (a) Dependent CO_2 reaction rate in $\text{CO}_2 + \text{H}_2$ and $\text{CO}_2 + \text{H}_2 + \text{EB}$ atmosphere over composite catalysts with different intimacy of oxide and zeolite components. Reaction conditions: 573 K, GHSV of mixture gas ($\text{CO}_2/\text{H}_2/\text{Ar} = 23:69:8$, vol%) = 3000 mL g⁻¹ h⁻¹, partial pressure is kept at 1.5 MPa with or without the introduction of EB, time on stream = 1 h. (b) Dependent performance of CO_2 hydrogenation in the presence of EB on the molar ratio of Si to Al. Reaction conditions: 633 K, 3 MPa, GHSV of a mixture gas ($\text{CO}_2/\text{H}_2/\text{Ar} = 23:69:8$, vol%) = 12,000 mL g⁻¹ h⁻¹, and WHSV of EB = 1 h⁻¹. (c) Schematic of CO_2 hydrogenation in the presence of EB over zeolites with the higher and lower acid density. (d) Optimized adsorption structures of methanol and EB. (e) Adsorption enthalpies (ΔH_{ads}) and free energies (ΔG_{ads}) calculated at 633 K. (f) Gibbs free energy profiles of the formation of SMS and methylation between SMS and EB at 633 K. (Blue balls: Si; red balls: O; white balls: H; pink balls: Al; gray balls: C) (g) Illustration of the controlled production of PetT from CO_2 hydrogenation in the presence of EB.

which the methoxy intermediates go through a rapid alkylation reaction with EB molecules rather than being subjected to participating into complex hydrogenation and dehydrogenation procedures.

We further performed the theoretical simulation to gain a thorough insight into the adsorption and transformation of the intermediates (Fig. 5d-f and Fig. S21). Both methanol and EB molecules can enter into the channels of ZSM-5 zeolite and adsorb onto the acid sites. The adsorption enthalpies (ΔH_{ads}) for EB and methanol at 633 K are calculated to be -133.3 and -120.5 kJ mol⁻¹, and the free energies of adsorption (ΔG_{ads}) are -29.2 and -23.1 kJ mol⁻¹, respectively. The difference in adsorption enthalpy between EB and methanol of 13 kJ mol⁻¹ implies that there should be a more favorable adsorption of EB in comparison with methanol (Fig. 5d-e). Focusing on the transformation of methanol in the zeolite channels, we find that the formation of SMS is feasible with Gibbs free energy barriers of 143.2 kJ mol⁻¹. Once the SMS species forms in the zeolite, it can methylate with EB to fulfill the efficient tandem reaction with a relative lower free energy barrier of 77.3 kJ mol⁻¹, much lower than that of direct C-C coupling between SMS (over 200 kJ mol⁻¹) [14,30] (Fig. 5f and Fig. S22-23). Such results further indicate that the facile formation and enrichment of SMS might be the key to efficient tandem reaction. It is different from the cases in direct conversion of methanol toward hydrocarbons, where the disparate controlling steps may account for the main processes. On the basis of these results, we can not only reiterate the facile C-C coupling in this system, which has been proposed according to the abundant experimental evidences mentioned above, but also solidly manifest the importance of the effect of intermediate transfer on the reaction kinetics.

In a word, we find out that the intermediate species transfer in both micro- and nano- scales plays a critical role in the establishment and

maintenance of a highly efficient aromatic hydrocarbon cycle continuously producing ET with excellent selectivity. Such effect could be readily manipulated by controlling the intimacy of active components and regulating the acid properties of zeolite, thus responsible for superior adjustability and attenuated activity-selectivity trade-off compared with conventional CO_x hydrogenation to aromatics processes (Fig. 5g).

4. Conclusions

A tandem catalytic system for CO_2 hydrogenation in the presence of EB has been established over a composite catalyst consisting of Zn-Zr oxide and HZSM-5 zeolite, and it achieves remarkable performance for synthesis of ethyl-toluene with a selectivity of $\sim 80\%$, in which the most valuable isomer *para*-ethyl-toluene accounts for $\sim 75\%$. Undesired CO is suppressed to $< 30\%$, as negligible non-aromatic C₅₊ hydrocarbons can be found in liquid products, suggesting the high efficiency of CO_2 utilization in tandem hydrogenation and alkylation. By means of various (*quasi-*) *in situ* characterization techniques, we clearly depict the reaction pathway and provide the solid evidence of the incorporation of CO_2 into the target products. More importantly, the evolution of the key methoxy intermediates, which bridge the different active components as well as the tandem reaction sequences, has also been unveiled. This process, in turn, helps us understand the effect of the intermediate transfer on the kinetically controlling steps and apparent catalytic performance at both micro- and nano- scales, thus rendering opportunities for optimizing a highly efficient aromatic hydrocarbon cycle toward targeted ethyl-toluene products via controlling the intimacy of components as well as regulating the acid properties. Such results not only offer a novel strategy to realizing the preferential synthesis of specific aromatics ethyl-toluene from CO_2 hydrogenation via tandem reactions, but

also are expected to inspire more comprehensive understanding of catalytic systems involving the integration of multiple active components and the conjunction of associated elementary steps.

CRediT authorship contribution statement

Su Xiong: Writing – review & editing, Supervision, Project administration. **Huang Yanqiang:** Writing – review & editing, Supervision. **Zhang Tao:** Supervision. **Shang Xin:** Writing – original draft, Methodology, Investigation, Formal analysis, Data curation. **Han Qiao:** Methodology, Data curation. **Zhang Wennan:** Software. **Wei Yingxu:** Supervision, Project administration. **Liu Guodong:** Supervision, Investigation, Formal analysis. **Hou Guangjin:** Supervision, Investigation.

Declaration of Competing Interest

The authors declare that they have no known competing financial interests or personal relationships that could have appeared to influence the work reported in this paper.

Data availability

Data will be made available on request.

Acknowledgments

The authors acknowledge the financial support from Strategic Priority Research Program of the Chinese Academy of Sciences (No. XDA29040600 and No. XDB36030200), CAS Project for Young Scientists in Basic Research (YSBR-022), National Natural Science Foundation of China (21978286, 21925803, U19A2015, 22325405, 22321002, 22002157, 22241801), Youth Innovation Promotion Association CAS, Young Top-notch Talents of Liaoning Province (XLYC2007082).

Appendix A. Supporting information

Supplementary data associated with this article can be found in the online version at [doi:10.1016/j.apcatb.2024.123833](https://doi.org/10.1016/j.apcatb.2024.123833).

References

- [1] C. Hepburn, E. Adlen, J. Beddington, E.A. Carter, S. Fuss, N. Mac Dowell, J.C. Minx, P. Smith, C.K. Williams, The technological and economic prospects for CO₂ utilization and removal, *Nature* 575 (2019) 87–97, <https://doi.org/10.1038/s41586-019-1681-6>.
- [2] X. Shang, G. Liu, X. Su, Y. Huang, T. Zhang, A review of the recent progress on direct heterogeneous catalytic CO₂ hydrogenation to gasoline-range hydrocarbons, *EES Catal.* 1 (2023) 353–368, <https://doi.org/10.1039/D3EY00026E>.
- [3] J. Wei, Q. Ge, R. Yao, Z. Wen, C. Fang, L. Guo, H. Xu, J. Sun, Directly converting CO₂ into a gasoline fuel, *Nat. Commun.* 8 (2017) 15174, <https://doi.org/10.1038/ncomms15174>.
- [4] J. Wei, R. Yao, Q. Ge, D. Xu, C. Fang, J. Zhang, H. Xu, J. Sun, Precisely regulating Brønsted acid sites to promote the synthesis of light aromatics via CO₂ hydrogenation, *Appl. Catal., B* 283 (2021) 119648, <https://doi.org/10.1016/j.apcatb.2020.119648>.
- [5] Y. Ni, Z. Chen, Y. Fu, Y. Liu, W. Zhu, Z. Liu, Selective conversion of CO₂ and H₂ into aromatics, *Nat. Commun.* 9 (2018) 3457, <https://doi.org/10.1038/s41467-018-05880-4>.
- [6] P. Gao, S. Li, X. Bu, S. Dang, Z. Liu, H. Wang, L. Zhong, M. Qiu, C. Yang, J. Cai, W. Wei, Y. Sun, Direct conversion of CO₂ into liquid fuels with high selectivity over a bifunctional catalyst, *Nat. Chem.* 9 (2017) 1019, <https://doi.org/10.1038/nchem.2794>.
- [7] Z. Li, Y. Qu, J. Wang, H. Liu, M. Li, S. Miao, C. Li, Highly selective conversion of carbon dioxide to aromatics over tandem catalysts, *Joule* 3 (2019) 570–583, <https://doi.org/10.1016/j.joule.2018.10.027>.
- [8] M. Koehle, E. Saraci, P. Dauenhauer, R.F. Lobo, Production of p-methylstyrene and p-divinylbenzene from furanic compounds, *ChemSusChem* 10 (2017) 91–98, <https://doi.org/10.1002/cssc.201601554>.
- [9] W.W. Kaeding, G.C. Barile, *Para-methylstyrene: a new commercial monomer for the styrenics industry*, in: B.M. Culbertson, C.U. Pittman (Eds.), *New Monomers and Polymers*, Springer US, Boston, MA, 1984, pp. 223–241.
- [10] C. Zhou, J. Shi, W. Zhou, K. Cheng, Q. Zhang, J. Kang, Y. Wang, Highly active ZnO-ZrO₂ aerogels integrated with H-ZSM-5 for aromatics synthesis from carbon dioxide, *ACS Catal.* 10 (2019) 302–310, <https://doi.org/10.1021/acscatal.9b04309>.
- [11] D. Miao, X. Pan, F. Jiao, Y. Ji, G. Hou, L. Xu, X. Bao, Selective synthesis of para-xylene and light olefins from CO₂/H₂ in the presence of toluene, *Catal. Sci. Technol.* 11 (2021) 4521–4528, <https://doi.org/10.1039/D1CY00602A>.
- [12] Y. Xu, C. Shi, B. Liu, T. Wang, J. Zheng, W. Li, D. Liu, X. Liu, Selective production of aromatics from CO₂, *Catal. Sci. Technol.* 9 (2019) 593–610, <https://doi.org/10.1039/C8CY02024H>.
- [13] J. Zuo, W. Chen, J. Liu, X. Duan, L. Ye, Y. Yuan, Selective methylation of toluene using CO₂ and H₂ to para-xylene, *Sci. Adv.* 6 (2020) eaba5433, <https://doi.org/10.1126/sciadv.eaba5433>.
- [14] J. Zuo, C. Liu, X. Han, D. Wen, X. Liu, L. Ye, W. Zhuang, Y. Yuan, Steering CO₂ hydrogenation coupled with benzene alkylation toward ethylbenzene and propylbenzene using a dual-bed catalyst system, *Chem. Catal.* 2 (2022) 1223–1240, <https://doi.org/10.1016/j.jchcat.2022.04.003>.
- [15] X. Shang, G. Liu, X. Su, Y. Huang, T. Zhang, Preferential synthesis of toluene and xylene from CO₂ hydrogenation in the presence of benzene through an enhanced coupling reaction, *ACS Catal.* 12 (2022) 13741–13754, <https://doi.org/10.1021/acscatal.2c04314>.
- [16] X. Shang, H. Zhuo, Q. Han, X. Yang, G. Hou, G. Liu, X. Su, Y. Huang, T. Zhang, Xylene synthesis through tandem CO₂ hydrogenation and toluene methylation over a composite ZnZrO zeolite catalyst, *Angew. Chem. Int. Ed.* 62 (2023) e202309377, <https://doi.org/10.1002/anie.202309377>.
- [17] Y. Liu, X. Zhou, X. Pang, Y. Jin, X. Meng, X. Zheng, X. Gao, F.-S. Xiao, Improved para-xylene selectivity in meta-xylene isomerization over ZSM-5 crystals with relatively long b-axis length, *ChemCatChem* 5 (2013) 1517–1523, <https://doi.org/10.1002/cctc.201200691>.
- [18] P. Magnoux, P. Roger, C. Canaff, V. Fouche, N.S. Gnepp, M. Guisnet, New technique for the characterization of carbonaceous compounds responsible for zeolite deactivation, in: B. Delmon, G.F. Froment (Eds.), *Stud. Surf. Sci. Catal.*, Elsevier, 1987, pp. 317–330.
- [19] D. Lesthaeghe, B. DeSterck, V. VanSpeybroeck, G.B. Marin, M. Waroquier, Zeolite shape-selectivity in the gem-methylation of aromatic hydrocarbons, *Angew. Chem. Int. Ed.* 46 (2007) 1311–1314, <https://doi.org/10.1002/anie.200604309>.
- [20] J.-D. Chai, M. Head-Gordon, Long-range corrected hybrid density functionals with damped atom–atom dispersion corrections, *Phys. Chem. Chem. Phys.* 10 (2008) 6615–6620, <https://doi.org/10.1039/B810189B>.
- [21] M.J.T. Frisch, G.W. Schlegel, H.B.; Scuseria, G.E.; Robb, M.A.; Cheeseman, J.R.; Scalmani, G.; Barone, V.; Mennucci, B.; Petersson, G.A.; Nakatsuji, H.; Caricato, M.; Li, X.; Hratchian, H.P.; Izmaylov, A.F.; Bloino, J.; Zheng, G.; Sonnenberg, J.L.; Hada, M.; Ehara, M.; Toyota, K.; Fukuda, R.; Hasegawa, J.; Ishida, M.; Nakajima, T.; Honda, Y.; Kitao, O.; Nakai, H.; Vreven, T.; Montgomery, J.A.; Peralta, J.E.; Ogliaro, F.; Bearpark, M.; Heyd, J.J.; Brothers, E.; Kudin, K.N.; Staroverov, V.N.; Kobayashi, R.; Normand, J.; Ragahavachari, K.; Rendell, A.; Burant, C.; Iyengar, S. S.; Tomasi, J.; Cossi, M.; Rega, N.; Millam, J.M.; Klene, M.; Knox, J.E.; Cross, J.B.; Bakken, V.; Adamo, C.; Jaramillo, J.; Gomperts, R.; Stratmann, R.E.; Yazyev, O.; Austin, A. J.; Cammi, R.; Pomelli, C.; Ochterski, J.W.; Martin, R.L.; Morokuma, K.; Zakrzewski, V.G.; Voth, G.A.; Salvador, P.; Dannenberg, J.J.; Dapprich, S.; Daniels, A.D.; Farkas, O.; Foresman, J.B.; Ortiz, J.; Cioslowski, J.; Fox, D. J. Gaussian 09, Revision B.01, Gaussian, Inc.: Wallingford, CT, 2010.
- [22] J. Wang, G. Li, Z. Li, C. Tang, Z. Feng, H. An, H. Liu, T. Liu, C. Li, A highly selective and stable ZnO-ZrO₂ solid solution catalyst for CO₂ hydrogenation to methanol, *Sci. Adv.* 3 (2017) e1701290, <https://doi.org/10.1126/sciadv.1701290>.
- [23] K. Cheng, W. Zhou, J. Kang, S. He, S. Shi, Q. Zhang, Y. Pan, W. Wen, Y. Wang, Bifunctional catalysts for one-step conversion of syngas into aromatics with excellent selectivity and stability, *Chem* 3 (2017) 334–347, <https://doi.org/10.1016/j.chempr.2017.05.007>.
- [24] S. Kattel, B. Yan, Y. Yang, J.G. Chen, P. Liu, Optimizing binding energies of key intermediates for CO₂ hydrogenation to methanol over oxide-supported copper, *J. Am. Chem. Soc.* 138 (2016) 12440–12450, <https://doi.org/10.1021/jacs.6b05791>.
- [25] Z. Qi, L. Chen, S. Zhang, J. Su, G.A. Somorjai, Mechanism of methanol decomposition over single-site Pt1/CeO₂ catalyst: a DRIFTS study, *J. Am. Chem. Soc.* (2020), <https://doi.org/10.1021/jacs.0c10728>.
- [26] Q. Han, P. Gao, K. Chen, L. Liang, Z. Zhao, X. Yao, D. Xiao, X. Han, G. Hou, Synergistic interplay of dual active sites on spinel ZnAl₂O₄ for syngas conversion, *Chem* 9 (2023) 721–738, <https://doi.org/10.1016/j.chempr.2023.01.004>.
- [27] Y. Ji, P. Gao, Z. Zhao, D. Xiao, Q. Han, H. Chen, K. Gong, K. Chen, X. Han, X. Bao, G. Hou, Oxygenate-based routes regulate syngas conversion over oxide-zeolite bifunctional catalysts, *Nat. Catal.* 5 (2022) 594–604, <https://doi.org/10.1038/s41929-022-00806-2>.
- [28] W. Wang, A. Buchholz, M. Seiler, M. Hunger, Evidence for an initiation of the methanol-to-olefin process by reactive surface methoxy groups on acidic zeolite catalysts, *J. Am. Chem. Soc.* 125 (2003) 15260–15267, <https://doi.org/10.1021/ja0304244>.
- [29] S. Lin, Y. Zhi, W. Chen, H. Li, W. Zhang, C. Lou, X. Wu, S. Zeng, S. Xu, J. Xiao, A. Zheng, Y. Wei, Z. Liu, Molecular routes of dynamic autocatalysis for methanol-to-hydrocarbons reaction, *J. Am. Chem. Soc.* 143 (2021) 12038–12052, <https://doi.org/10.1021/jacs.1c03475>.
- [30] S. Ilias, A. Bhan, Mechanism of the catalytic conversion of methanol to hydrocarbons, *ACS Catal.* 3 (2012) 18–31, <https://doi.org/10.1021/cs3006583>.
- [31] Y. Li, M. Wang, S. Liu, F. Wu, Q. Zhang, S. Zhang, K. Cheng, Y. Wang, Distance for communication between metal and acid sites for syngas conversion, *ACS Catal.* 12 (2022) 8793–8801, <https://doi.org/10.1021/acscatal.2c02125>.
- [32] X. Yang, T. Sun, J. Ma, X. Su, R. Wang, Y. Zhang, H. Duan, Y. Huang, T. Zhang, The influence of intimacy on the ‘iterative reactions’ during OX-ZEO process for

aromatic production, J. Energy Chem. 35 (2019) 60–65, <https://doi.org/10.1016/j.jechem.2018.11.003>.